Journal of Materials Science: Materials in Electronics (2020) 31:5176–5186
https://doi.org/10.1007/s10854-020-03077-4

Hydrothermal synthesis and photo-Fenton degradation of magnetic $MnFe_2O_4$/rGO nanocomposites

Zhiqiang Wei[1] · Shangpan Huang[1] · Xudong Zhang[1] · Chenggong Lu[1] · Yongjia He[2]

Received: 13 November 2019 / Accepted: 10 February 2020 / Published online: 19 February 2020

Abstract
Magnetic recoverable $MnFe_2O_4$/rGO nanocomposites were synthesized via a facile one-pot hydrothermal method. The microstructure, morphology, optical and magnetic property were characterized by X-ray diffraction, high-resolution transmission electron microscope, ultraviolet–visible spectroscopy, N_2 adsorption–desorption technique, photoluminescence spectroscopy and vibrating sample magnetometer. The photo-Fenton degradation activity of the $MnFe_2O_4$/rGO composites was investigated using the methylene blue (MB) in aqueous solution under the simulated sunlight. The results show that $MnFe_2O_4$ nanoparticles with cubic spinel structure were loaded on the surface of rGO, possessing irregular ellipsoid with uniform particle size and good dispersion. The band gap of $MnFe_2O_4$/rGO is narrower than that of pure $MnFe_2O_4$ and exhibits redshift. The weak luminescence of $MnFe_2O_4$/rGO nanocomposites indicates the efficient separation of photoexcited electron/hole pairs. $MnFe_2O_4$/rGO nanocomposites display superior photo-Fenton degradation efficiency of MB, exhibit obvious room temperature ferromagnetism and can be readily recovered by external magnetic field. $MnFe_2O_4$/rGO nanocomposites exhibit the best degradation efficiency under the condition of pH 9, 0.5 mL H_2O_2 and 0.06 g mass fraction in photo-Fenton degradation of MB dye. The radical scavenger tests demonstrate that ·OH, e^- and h^+ are the main active species and play a decisive role, and rGO plays a vital role in synergistic enhancement of photo-Fenton degradation.

1 Introduction

In recent decades, environmental pollution and energy shortage have become global problem facing mankind due to the rapid growth of population and the development of modern industry [1–3]. Meanwhile, it is difficult to degrade the toxic, chromatic and organic dye wastewater under natural conditions. Up to now, various physicochemical methods including adsorption membrane filtration, biodegradation, chemical oxidation and photocatalytic degradation have been developed to eliminate toxic pollutants in wastewater [4–8]. Among them, the photocatalytic degradation technology widely spread in the removal of organic matter under mild reaction conditions, which is considered to be one of the most promising approaches because it is efficient, low cost and friendly environment, especially the conversion of light energy into chemical energy [9–11]. Moreover, the process of photocatalytic degradation requires no additional additives and equipment, except light that is inexhaustible in nature [12–14]. Therefore, it is urgent to develop more ideal photocatalytic materials to degrade organic pollutants in wastewater and meet the sustainable development of human society.

$MnFe_2O_4$ as a kind of bimetal oxide semiconductor nanomaterial shows excellent photocatalytic performance in photocatalytic degradation of organic synthetic dyes and pigments in wastewater, which have been extensively investigated due to its unique spinel crystal, narrow band gap, visible light response, high chemical and thermal stabilities [15–17]. The electrical transport of $MnFe_2O_4$ accelerates the effect of Verway hopping: $Mn^{2+} + Fe^{3+} \leftrightarrow Mn^{3+} + Fe^{2+}$, and the electron transfer between a mixed valance Mn^{2+} and Fe^{3+} on octahedral sites to enhance the photo-Fenton activity [18, 19]. In addition, $MnFe_2O_4$ can be effectively separated and recovered by external magnetic field with high recycling efficiency due to room temperature ferromagnetism [20–23]. However, the photocatalytic performance of pure $MnFe_2O_4$ is not high enough due to the fast recombination of photogenerated electron–hole pairs, which seriously affects

✉ Zhiqiang Wei
qianweizuo@163.com

[1] School of Science, Lanzhou University of Technology, Lanzhou 730050, China

[2] State Key Laboratory of Silicate Materials for Architectures, Wuhan University of Technology, Wuhan 430070, China

it difficult to further promote and apply in photocatalysis [24–26]. Therefore, the photocatalytic activity of $MnFe_2O_4$ are needed to improve by surface modification and hybridization to solve the recombination of photogenerated electron–hole pairs.

As a new two-dimensional carbon material, graphene is composed of single-layer carbon atoms with two-dimensional planar structure, exhibiting many remarkable properties, such as large surface area, excellent electrical and mechanical properties [27–31]. Based on these unique properties, many researchers have attempted to modify metal oxide with graphene owing to fact that the composite materials can decrease the band gap and promote the separation and transfer of electrons and holes [32–35]. In addition, graphene coupling with good electrical conductivity can reduce the recombination probability of electrons and holes, improving its photocatalytic efficiency [20, 36–38]. Mishra et al. prepared rGO/$MnFe_2O_4$ nanocomposites by hydrothermal method with a different weight ratio of GO sheets, and studied the effect of the content of the GO sheets on the structural, optical, magnetic and microwave magnetic properties of $MnFe_2O_4$ nanoparticles [36]. Huang et al. reported solvothermal synthesis of magnetically separable rGO/$MnFe_2O_4$ hybrids as efficient photocatalysts for degradation of MB under visible light, and found with the increasing weight ratio of rGO content in the rGO/$MnFe_2O_4$ hybrids, the particle size of $MnFe_2O_4$ was gradually reduced but the visible light adsorption increased, and 10% rGO/$MnFe_2O_4$ hybrid exhibited the best photocatalytic activity [35]. Peng et al. synthesized magnetic recoverable graphene/$MnFe_2O_4$ hybrids for efficient decomposition of methylene blue, and found that rGO /$MnFe_2O_4$ catalyst shows exceptional performance towards the MB decomposition in the presence of H_2O_2, and the catalysts can be magnetically recycled [23]. The better catalytic performance of rGO/$MnFe_2O_4$ hybrid is mainly related to the synergetic effects of rGO, $MnFe_2O_4$, H_2O_2 and MB molecules, and it is also attributed to the redox couples of Fe/Mn ions in the reaction process. Unfortunately, to the best of our knowledge, up to now, most of the studies were focused on the photocatalytic activity, optical and magnetic property of the spinel structure mix-metal-oxide semiconductor, and there are few studies on the influence of pH value, dosage of photocatalyst and volume of H_2O_2 in the solution on the photo-Fenton degradation of organic synthetic dyes under simulated solar irradiation. From the perspective of industrial applications, it is necessary to evaluate the photo-Fenton degradation rate by controlling the pH value, amount of photocatalyst and volume of H_2O_2, in order to explore the photo-Fenton degradation mechanism and obtain the optimal photo-Fenton condition.

In this paper, magnetic recoverable $MnFe_2O_4$/rGO nanocomposites were successfully fabricated via a facile one-pot hydrothermal method, and the microstructure, morphology, optical and magnetic property of the samples were characterized by X-ray diffraction (XRD), high-resolution transmission electron microscopy (HRTEM), ultraviolet–visible spectroscopy, N_2 adsorption–desorption technique, photoluminescence spectra (PL) and vibrating sample magnetometer (VSM). The photo-Fenton activity of the samples was evaluated by the photodegradation of methylene blue (MB) in aqueous solution under the simulated sunlight, the effects of pH value, dosage of photocatalyst and volume of H_2O_2 on the photo-Fenton degradation were studied, and the possible photo-Fenton mechanism was further proposed.

2 Experimental

2.1 Preparation of $MnFe_2O_4$–rGO nanocomposites

All chemicals were analytical grade without any further purification. Graphene oxide (GO) was synthesized from natural graphite powder via a modified Hummers method [39]. Firstly, 1 g of graphite powder was weighed and 23 mL concentrated H_2SO_4 was added to a 500 mL three-necked round bottom bottle; the mixture was kept in an ice-water bath to ensure the temperature remained below 5 ℃. Then, 5 g $KMnO_4$ was slowly added into the mixed solution under constant magnetic stirring for 2 h in order to make concentrated H_2SO_4 fully inserted into the graphite layer. The mixture was oxidized for 1 h at 35 ± 5 °C, and 150 mL deionized water was added and then stirred at 98 °C for 15 min. Finally, 5 mL of 30% hydrogen peroxide was added in the mixed solution to terminate the reaction mixture. Then, the mixed solution was filtered and washed by adding 200 mL 5% hydrochloric acid solution. After repeated centrifugation to neutral, ultrasonication was carried out for 4 h to finally obtain graphene oxide.

$MnFe_2O_4$ nanoparticles were synthesized by one-step hydrothermal method. In a typical procedure, 2.5 mmol $MnCl_2{\cdot}4H_2O$ and 5 mmol $FeCl_3{\cdot}6H_2O$ were weighed as precursors, and dissolved in ethylene glycol to obtain 0.05 mol/L mixed metal salt solution by magnetic stirring at room temperature. Meanwhile, NaOH solution (0.5 mol/L) was added dropwise into the above solution to regulate the pH value of the mixed solution to 12. Subsequently, 1 g PVP slowly was added to the above mixed solution under constant magnetic stirring. The resultant mixture was then transferred to seal into a 100 mL Teflon-lined stainless-steel autoclave and kept at 200 °C for 24 h. After the reaction was completed, the autoclave was naturally cooled down to room temperature. Thereafter, the resulting precipitate was separated centrifugally and washed several times with distilled water and absolute alcohol to remove excess surfactants and impurities, respectively, and dried at 60 ℃ in a vacuum oven for 12 h. For comparison, $MnFe_2O_4$/rGO (with weight

percent of GO to the total mass ratio of 10%) was prepared under the same hydrothermal condition of $MnFe_2O_4$ sample, as shown in Fig. 1, except that GO slurry was added dropwise to the mixed solution under ultrasonic treatment to obtain a uniform mixture.

2.2 Characterization

The structural analysis of the as-prepared samples was examined by a powder X-ray diffractometer (Rigaku corporation, Japan, D/Max-2400) with Cu Kα radiation at = 1.54056 Å. The samples were scanned in the angular range from 10° to 70° with scanning rate of 0.005°/s and step size of 0.02°. The morphology and microstructure were characterized by high-resolution transmission electron microscopy (HRTEM, JEM-2010). The recombination rates of electron–hole pairs were characterized by photoluminescence spectra (PL). The band gap energy was characterized by UV–Vis spectrophotometer (PERSEE TU-1901) with an integrating sphere attachment. Magnetic hysteresis loops were investigated at room temperature using a vibrating sample magnetometer (VSM, Lakeshore 7304). The Brunaue–Emmett–Teller (BET) specific surface area and Barrett–Joyner–Halenda (BJH) pore size distribution of the samples were tested by N_2 adsorption–desorption technique using an ASAP 2020 analyzer.

2.3 Photo-Fenton experiment

The photo-Fenton degradation experiments were performed in VS-GCH-XE-300 photochemical reaction apparatus at room temperature. The synthesized $MnFe_2O_4$/rGO composite was employed as photocatalyst to degrade MB dye under the simulated sunlight irradiation. In a typical experiment, a certain amount of catalyst was dispersed in 100 mL MB solution, and pH of the mixed solution adjusted to a certain value. Meanwhile, the distance between the light source and the catalysts was fixed at 15 cm. The suspension was firstly ultrasonicated for 10 min, and then magnetically stirred in the dark for 30 min before illumination to establish adsorption–desorption equilibrium between photocatalyst and MB dye. Subsequently, 0.5 mL H_2O_2 was added to the MB dye solution under the simulated sunlight. Among them, the photo-Fenton reaction was carried out for 150 min under 300W xenon lamp irradiation with different masses of catalyst and different pH values. Subsequently, 4 mL of the reaction solution was taken out at given time intervals (30 min). The concentration of MB dye was determined by measuring the absorbance of the solution at a fixed wavelength of $\lambda = 664$ nm using a UV–Vis spectrophotometer during the photo-Fenton process. The samples were subjected to stability and cycle tests with magnetically collected and separated.

3 Results and discussion

The typical XRD pattern of GO, $MnFe_2O_4$ and $MnFe_2O_4$/rGO nanocomposites is shown in Fig. 2. The diffraction peak of GO appeared at $2\theta = 11.81°$ corresponds to the crystal plane of (001) [40]. In the process of graphite powder oxidation, the increase of oxygen functional group leads to the increase of crystal surface spacing of graphite layer. Compared with pure $MnFe_2O_4$, the XRD pattern of $MnFe_2O_4$/rGO nanocomposite shows obvious diffraction peak of rGO at $2\theta = 23.2°$, but no characteristic peak of GO was observed. It demonstrated that the decreased graphite layer spacing would result in GO being reduced to rGO due to the removal of some oxygen-containing functional groups in the

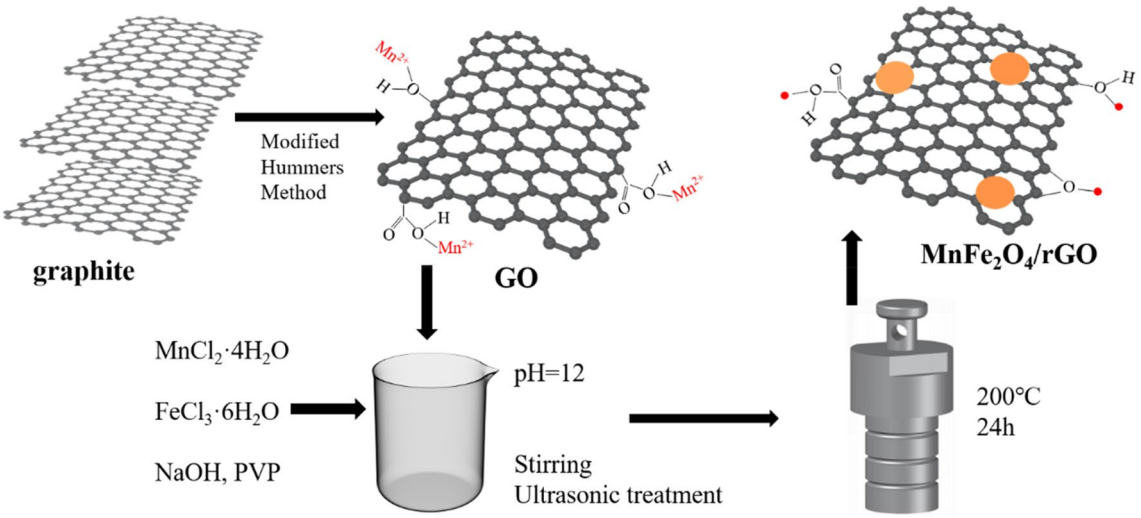

Fig. 1 Schematic diagram of the synthesis procedure of $MnFe_2O_4$/rGO nanocomposites

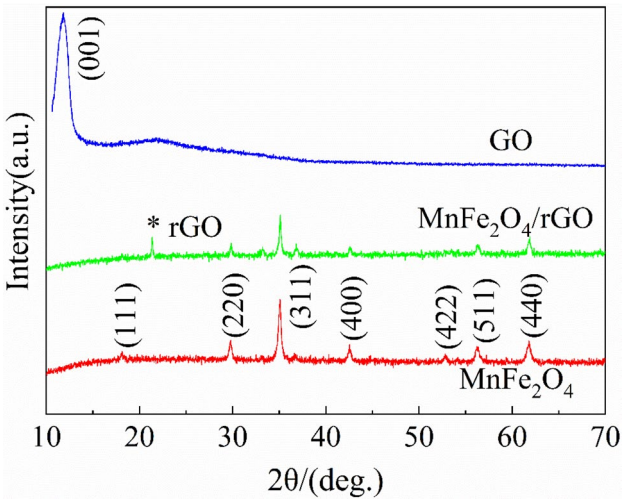

Fig. 2 XRD patterns of GO, $MnFe_2O_4$ and $MnFe_2O_4$/rGO

Table 1 Crystallite size, specific surface area and pore parameters of $MnFe_2O_4$ and $MnFe_2O_4$/rGO

Samples	Crystallite size (nm)	S_{BET} (m^2/g)	Average pore size (nm)	V_{Pore} (cm^3/g)
$MnFe_2O_4$	70	26	10.9	0.13
$MnFe_2O_4$/rGO	65	33	14.7	0.08

hydrothermal reaction process [41]. The XRD patterns of $MnFe_2O_4$ and $MnFe_2O_4$/rGO samples possess similar diffraction peaks at $2\theta = 18.077°$, 29.789°, 35.034°, 42.505°, 52.907°, 56.246° and 61.799°, completely corresponding to the (111), (220), (311), (400), (422), (511) and (440) crystal planes of spinel structure $MnFe_2O_4$ with JPCDS (No. 10-0319), respectively. In addition, the $MnFe_2O_4$ (311) peak is much higher than any other peak, which concludes that the as-synthesized $MnFe_2O_4$ nanomaterials are well crystallized and grew along the crystal planes (311). The crystallite size is estimated from the most intense diffraction peak (311) based on Scherrer equation to be 70 and 65 nm for pure $MnFe_2O_4$ and $MnFe_2O_4$/rGO nanocomposites, respectively (shown in Table 1), which is consistent with the HRTEM results.

The morphology and microstructure of the samples were characterized by HRTEM. It can be seen that the morphology of pure $MnFe_2O_4$ is mainly irregular ellipsoidal with rough surface and irregular edges as shown in Fig. 3a. $MnFe_2O_4$ nanoparticles present different degrees of agglomeration owing to the van der Waals force, Coulomb force or chemical bond cooperation between nanoparticles. The histogram corresponding to the particle size distribution of pure $MnFe_2O_4$ is shown in Fig. 3b. It is obvious that the particle size mainly distributed in the range of 60–90 nm with relatively uniform and the average particle size about 75 nm. The selected area electron diffraction (SAED) pattern of pure $MnFe_2O_4$ is shown in Fig. 3c, and a series of concentric rings with different radii appear in the diffraction pattern due to the random orientation between grains, indicating that the sample possesses polycrystalline structure. The polycrystalline diffraction ring corresponds to the (111), (220), (311), (400), (422), (511) and (440) crystal plane of $MnFe_2O_4$ from inside to outside. The SAED and HRTEM results further show that pure $MnFe_2O_4$ is spinel structure, which is consistent with the XRD analysis results. Figure 3d represents the high magnification of the local part of pure $MnFe_2O_4$, which reveals that the fringes of $MnFe_2O_4$ with an interplanar spacing of about 0.256 nm are well crystallized and grew selectively along the (311) crystal planes of cubic spinel structure.

Figure 4a shows the HRTEM image of GO. Obviously, the prepared GO possesses transparent two-dimensional planar structure with single or few layers about tens of micrometers in area. There are some folds and wrinkles presented on the surface of GO film. It is seen that $MnFe_2O_4$ particles with irregular particle morphology are partially wrapped or completely covered by graphene, indicating that the surface activity and agglomeration between $MnFe_2O_4$ nanoparticles are inhibited by graphene coating. The good dispersion and no obvious agglomeration of $MnFe_2O_4$ nanoparticles are beneficial to the transfer photocarrier and improve the photocatalytic activity.

The band gap and absorption coefficient of the synthesized samples are the critical parameters for the photocatalytic degradation of pollutants, which was studied by UV–Vis absorption spectra. Figure 5a shows the UV–Vis absorption spectra of $MnFe_2O_4$ and $MnFe_2O_4$/rGO recorded in range 200–850 nm. Compared with pure $MnFe_2O_4$ nanoparticles, $MnFe_2O_4$/rGO nanocomposites reveal much higher absorption band in visible light region, manifesting that nanocomposites have strong absorption property in the visible region. For direct band gap, the absorption coefficient and band gap of the samples can be calculated according to Tauc formula [42]: $[\alpha h\nu]^2 = A(h\nu - E_g)$, where α, $h\nu$, A and E_g represent the absorption coefficient, the photon energy, constant dependent on the effective masses of electron–hole pairs and material refractive index and the band gap of materials, respectively. The relationship between $(\alpha h\nu)^2$ and $h\nu$ is represented in the inset of Fig. 5b. The band gap values (E_g) are obtained by extrapolating the linear region of the curve on $h\nu$ axis at $(\alpha h\nu)^2 = 0$ [43]. The estimated optical band gap E_g of pure $MnFe_2O_4$ and $MnFe_2O_4$/rGO nanocomposites are 2.44 eV and 2.13 eV, respectively. It is obvious that the band gap of $MnFe_2O_4$/rGO nanocomposites is smaller than that of pure $MnFe_2O_4$, and red shift occurs. This result is because $MnFe_2O_4$ nanoparticles are encased in graphene and trapped in a very small space in the core–shell structure, and the

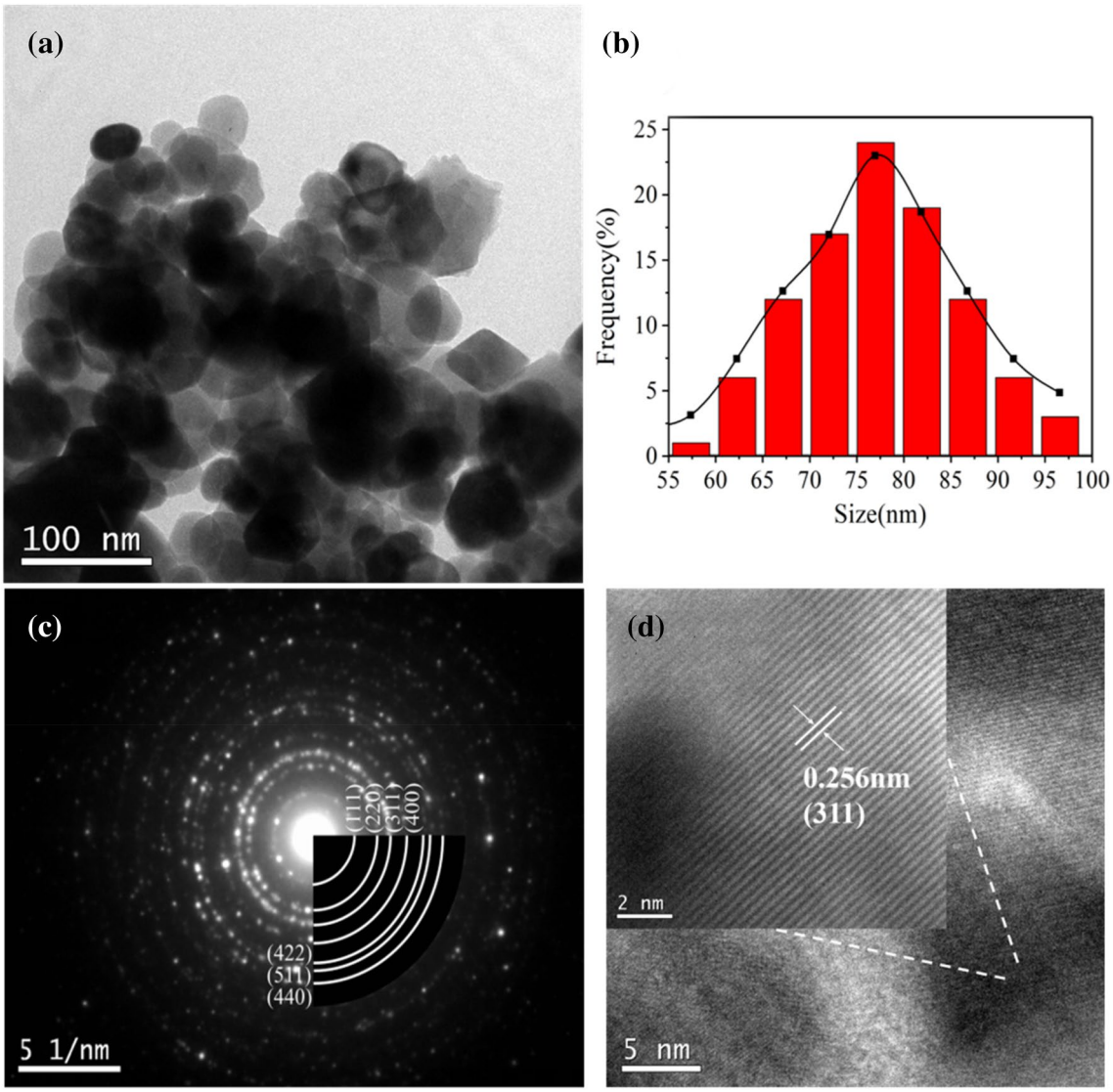

Fig. 3 HRTEM image (**a**); the corresponding particle size distribution (**b**); SAED pattern (**c**) and the partial enlarged HRTEM image (**d**) of pure $MnFe_2O_4$

surface effect of nanocrystals causes electron transition, narrowing the energy gap, and the light absorption band moves to the direction of long wave, thus widening the absorption intensity of $MnFe_2O_4$, which promotes the generation of more photoinduced electron–hole pairs, thereby increasing the photocatalytic activity.

The hysteresis loop of $MnFe_2O_4$ and $MnFe_2O_4$/rGO samples at room temperature with a magnetic field of − 20,000 Oe−20,000 Oe is shown in Fig. 6. The M–H curve shows that obvious hysteresis loops at room temperature, demonstrating $MnFe_2O_4$ and $MnFe_2O_4$/rGO nanomaterials possess room temperature ferromagnetism. The general formula of $MnFe_2O_4$ normal spinel structure is AB_2O_4, and the A position represents the tetrahedral position occupied by the divalent metal ion (Mn^{2+}) and the tetrahedral gap formed by the surrounding of four oxygen ions. Position B represents the octahedral space occupied by the trivalent metal ions (Fe^{3+}), which is surrounded by six oxygen ions. When the particle size reaches the nanoscale scale, the cation distribution in $MnFe_2O_4$ nanocrystals changes significantly, some Fe^{3+} enters the A position of tetrahedron, and Mn^{2+} enters the B position of octahedron, leading to the generation of ion logarithm of super exchange between A and B, which weakened spin coupling and ferromagnetism [44]. The magnetization intensity reaches saturation with the increase of magnetic field, which can effectively separate the catalyst for improving the recycling efficiency (inset of Fig. 6).

Figure 7a presents the N_2 adsorption–desorption isotherm of pure $MnFe_2O_4$ and $MnFe_2O_4$/rGO nanocomposites. The isotherms of all the samples in this work can be classified as

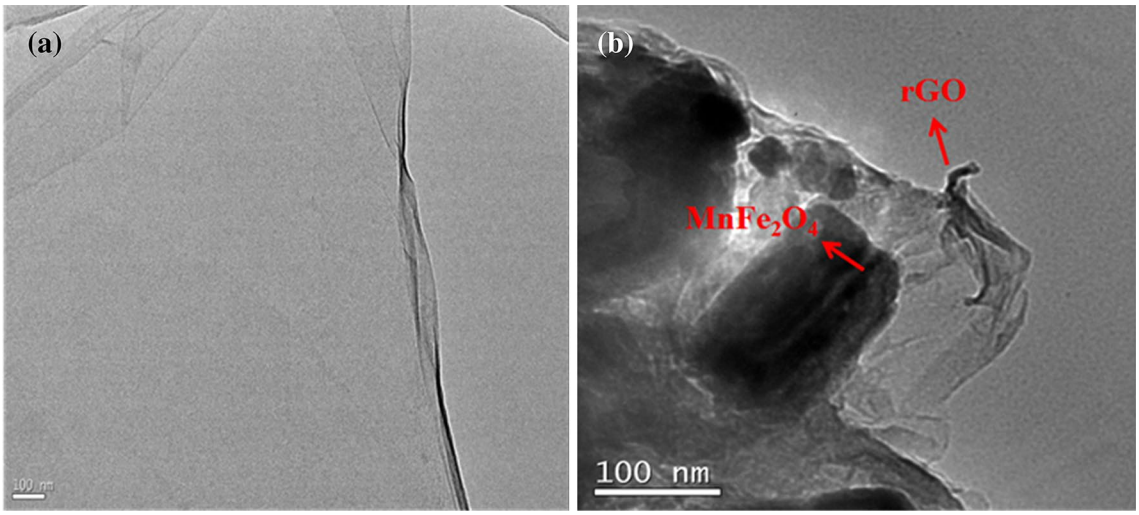

Fig. 4 HRTEM images of GO (**a**) and $MnFe_2O_4$/rGO (**b**)

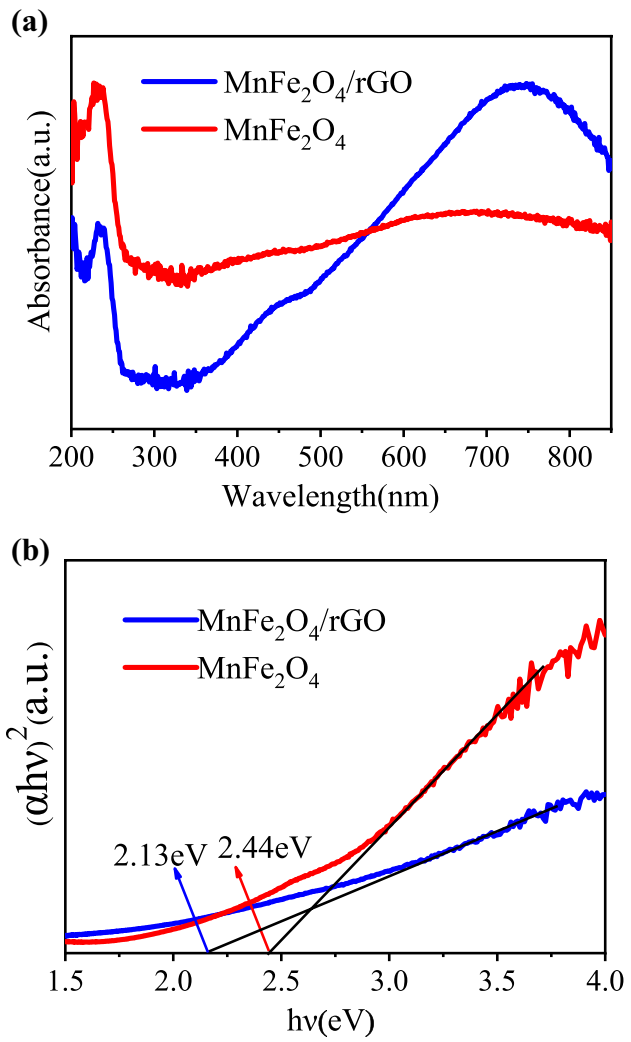

Fig. 5 UV–Vis absorption spectra (**a**) and the $(\alpha h\nu)^2$ versus $h\nu$ curves (**b**) of $MnFe_2O_4$ and $MnFe_2O_4$/rGO

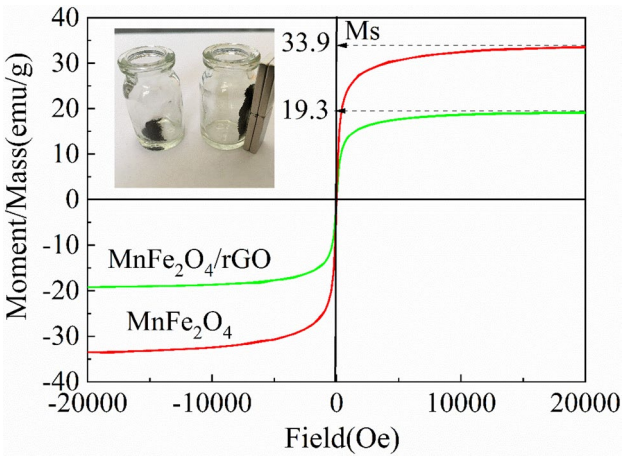

Fig. 6 Hysteresis loops of $MnFe_2O_4$ and $MnFe_2O_4$/rGO

type IV with H3 hysteresis loop at higher relative pressure according to the IUPAC classification, which indicates the obvious mesoporous structure characteristics. The BJH pore size distribution plot of pure $MnFe_2O_4$ and $MnFe_2O_4$/rGO nanocomposites is shown in Fig. 7b, which demonstrated that the pore diameter primarily distributed in the range of 3–50 nm within the typical mesoporous region for all the samples. The accumulated pore volume (V_{Pore}) and the average pore size of the samples are obtained from N_2 adsorption branch by the BJH method. The BET specific surface area (S_{BET}) of the samples is estimated from the linear region of the plot ranging from $P/P0 = 0.07$ to $P/P0 = 0.30$, and the specific surface area, total pore volume and pore width data are summarized in Table 1. The specific surface areas of $MnFe_2O_4$/rGO nanocomposites are larger than that of pure $MnFe_2O_4$, which partly attributed to $MnFe_2O_4$/rGO nanoparticles that are evenly wrapped in thin graphene sheets. The

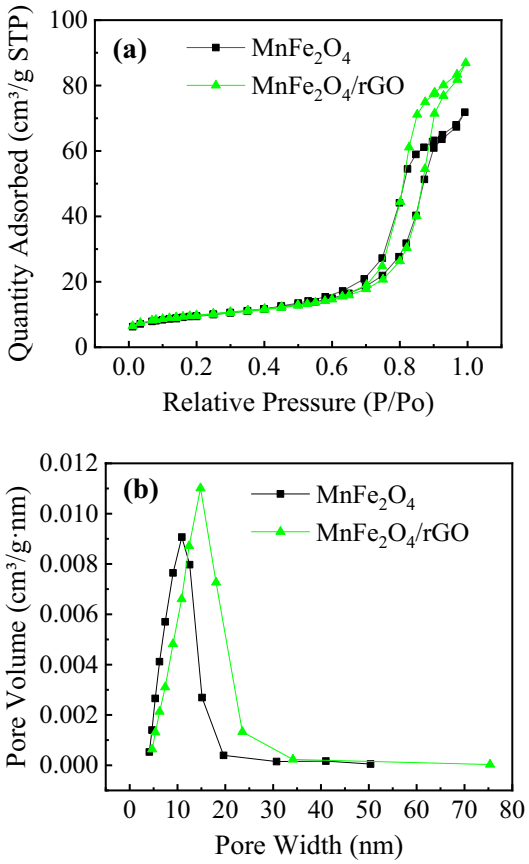

Fig. 7 N_2 adsorption–desorption isotherm (**a**) and pore size distribution plot (**b**) of $MnFe_2O_4$ and $MnFe_2O_4$/rGO

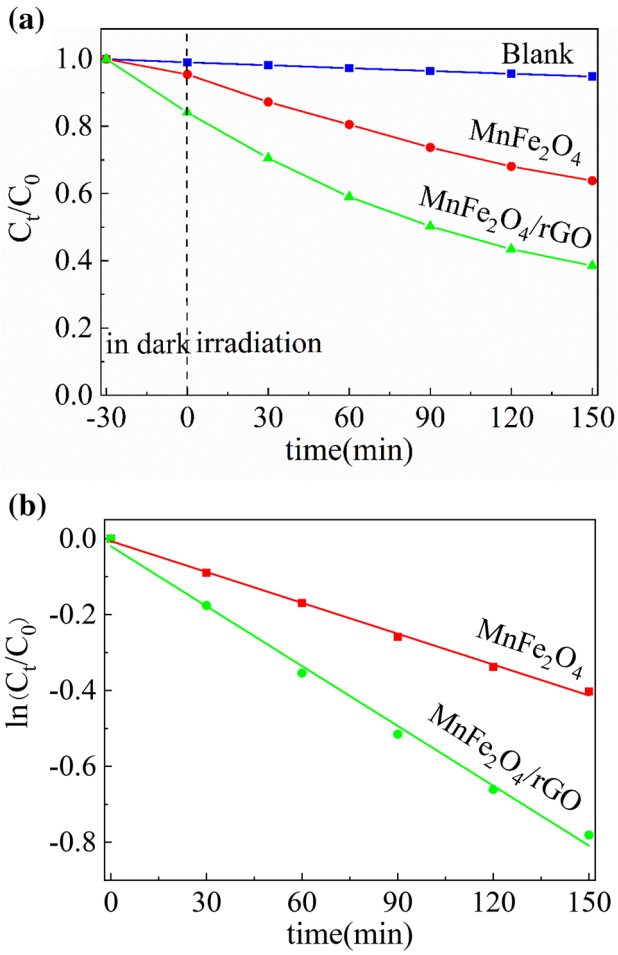

Fig. 8 The photo-Fenton degradation of MB over time (**a**) and plots of ln (C_t/C_0) vs irradiation time (**b**) for pure $MnFe_2O_4$ and $MnFe_2O_4$/rGO

increase of specific surface areas of $MnFe_2O_4$/rGO nanocomposites is beneficial to the photocatalytic performance of the photocatalyst.

Figure 8a shows the photo-Fenton degradation experiment of pure $MnFe_2O_4$ and $MnFe_2O_4$/rGO nanocomposite with 0.04 g catalysts, 0.5 mL H_2O_2 and normal conditions under simulated solar irradiation within 150 min. The blank experiment without any photocatalysts show that the self-degradation of MB is negligible, revealing that MB exhibits good stability without catalyst. The degradation percentage of the dye is defined as $(C_0 - C_t)/C_0 \times 100\%$, where C_0 and C_t represent the dye concentrations before and after t min of photocatalysis, respectively. Notably, the adsorption percentage of $MnFe_2O_4$/rGO nanocomposite (15%) exhibits a slightly increased adsorption compared to that of pure $MnFe_2O_4$ (6%) treatment in dark for 30 min. However, the degradation rate of MB increased with the increase of degradation time under simulated solar irradiation and catalyst acted together, implying that the continuous decrease of MB concentration was mainly caused by photocatalysis. It can be seen that the photo-Fenton degradation for $MnFe_2O_4$/rGO nanocomposite to MB solution under normal conditions is about 62% within 150 min. In contrast, the pure $MnFe_2O_4$ only removed about 36% of the initial concentration of MB solution. The improved photocatalytic performance of $MnFe_2O_4$/rGO composite significantly is mainly attributed to the high dispersibility of the high specific surface area of $MnFe_2O_4$ nanoparticles. Meanwhile, $MnFe_2O_4$ nanoparticles are on the rGO surface to facilitate separation and transfer of electron and holes. Figure 8b shows plots of ln (C_t/C_0) vs irradiation time t for the photo-Fenton degradation of $MnFe_2O_4$ and $MnFe_2O_4$/rGO composites corresponding to Fig. 8a. The kinetics of the photo-Fenton degradation to MB solution are conformed by first-order kinetic equation [7]: $\ln(C_t/C_0) = kt$ of $MnFe_2O_4$ and $MnFe_2O_4$/rGO composites, where k is reaction rate constant, t represents time, and C_0 and C_t represent the initial concentration and reaction concentration of MB, respectively. The rate constant k of $MnFe_2O_4$ and $MnFe_2O_4$/rGO is 0.00271/min and 0.00526/min, respectively. The $MnFe_2O_4$/rGO composites exhibit a photocatalytic activity about 2 times higher than that of

bare $MnFe_2O_4$ under normal conditions, which suggests that $MnFe_2O_4$/rGO is an excellent photocatalyst. In addition, the photogenerated electrons of $MnFe_2O_4$ would transfer from the conduction band of $MnFe_2O_4$ to rGO film, while rGO can reduce the optical band gap of $MnFe_2O_4$, enhancing sunlight absorption and the generation of electron–hole pair. Also, rGO acts as electron acceptor can inhibit the recombination of electron–hole pairs, thus accelerating redox reactions and promoting photodegradation of MB.

For the photo-Fenton degradation of MB dye, the amount of photocatalyst in the solution is an important factor. The effect of different amounts of $MnFe_2O_4$/rGO for the degradation of MB dye under simulated solar irradiation at pH 9 and 0.5 mL H_2O_2 within 150 min is shown in Fig. 9a. The degradation rates of MB were 62%, 69%, 73%, 76%, 80% and 78% by adding 0.040, 0.045, 0.050, 0.055, 0.060 and 0.065 g photocatalyst, respectively. It can be seen that the degradation rate of MB increased significantly when the photocatalyst dosage increased from 0.040 to 0.06 g, while the degradation rate decreased gradually when the photocatalyst dosage increased from 0.060 to 0.065 g, and the degradation rate increased to its maximum at 0.06 g. This results because

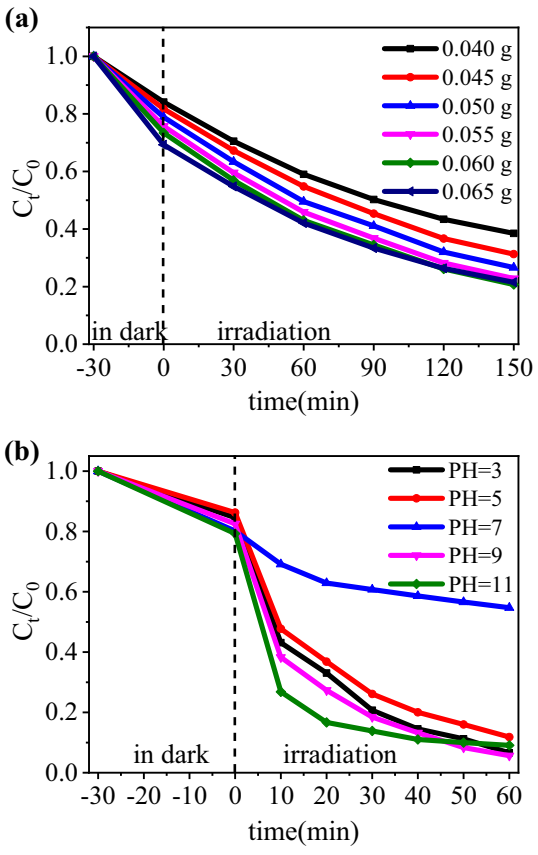

Fig. 9 Time-dependent photo-Fenton degradation of MB with different amounts of $MnFe_2O_4$/rGO composite (**a**) and with different pH values (**b**)

more active centers are added on the catalyst surface with the increase of photocatalyst consumption. However, as the amount of photocatalyst continues to increase, the turbidity of the reaction solution will also increase, thus reducing the utilization of visible light in photocatalytic reaction, which is unfavorable to photocatalytic degradation.

In the experiment, pH value also is a key factor to affect the photo-Fenton degradation of the catalyst. 0.06 g $MnFe_2O_4$/rGO with 0.5 mL H_2O_2 is chosen to measure the photo-Fenton degradation rate at different pH values within 60 min as shown in Fig. 9b. The degradation rates of MB were 93%, 88%, 45%, 95% and 91% when the pH values were 3, 5, 7, 9 and 11, respectively. It can be seen that the photo-Fenton degradation at pH 9 is the best. Under alkaline conditions, the photo-Fenton degradation rate of $MnFe_2O_4$/rGO composite is more efficient than neutral conditions, which maybe owing to H_2O_2 and NaOH have a slight reaction to produce O_2; O_2 is more likely to react with h^+ and generate·O^{2-}, speeding up the photocatalytic effect.

In order to evaluate the cyclic stability of the photocatalyst, the cycling stability of $MnFe_2O_4$/rGO photocatalyst for the degradation of MB dye under normal conditions with 0.04 g catalysts and 0.5 mL H_2O_2 for 5 successive cycles is shown in Fig. 10a. There is no obvious decrease of degradation rate after 5 cycles, indicating that the $MnFe_2O_4$/rGO photocatalyst exhibits higher stability and repeatability. Figure 10b shows the supernatant obtained by magnetite separation every 30 min in the first cycle. It can be clearly seen that the color of supernatant gradually becomes lighter with the increasing degradation time. Especially, MB dye becomes almost transparent after 150 min irradiation.

The active species are investigated to reveal the possible reaction mechanism. Here, we use 10 mL iso-propyl alcohol (IPA), 0.1 mmol $AgNO_3$, 10 mL methanol and 0.1 mmol parabenzoquinone (PBQ) to capture for hydroxyl radical (·OH), photogenic electron (e^-), hole (h^+) and superoxide radical (·O^{2-}), respectively [45]. Figure 11 shows the effects of different capture agents IPA, $AgNO_3$, methanol and PBQ on the photo-Fenton degradation of MB dye over $MnFe_2O_4$/rGO photocatalyst under simulated sunlight irradiation. It is noted that the photo-Fenton degradation rates of $MnFe_2O_4$/rGO decreased from 73 to 32%, 35%, 40% and 64% after adding the capture agents of IPA, $AgNO_3$, methanol and PBQ, respectively. It demonstrates that ·OH, e^- and h^+ are the main active species and play decisive role in $MnFe_2O_4$/rGO composite. While the photo-Fenton degradation rates of the dye are still 64% by adding the PBQ, which illustrates that ·O_2^- is not the active species.

Photoluminescence spectrum (PL) of photocatalysts is an effective means to study the recombination probability of photogenic electron–holes. Figure 12 shows a representative PL spectrum of pure $MnFe_2O_4$ and $MnFe_2O_4$/rGO with excitation wavelength is 300 nm. A strong emission

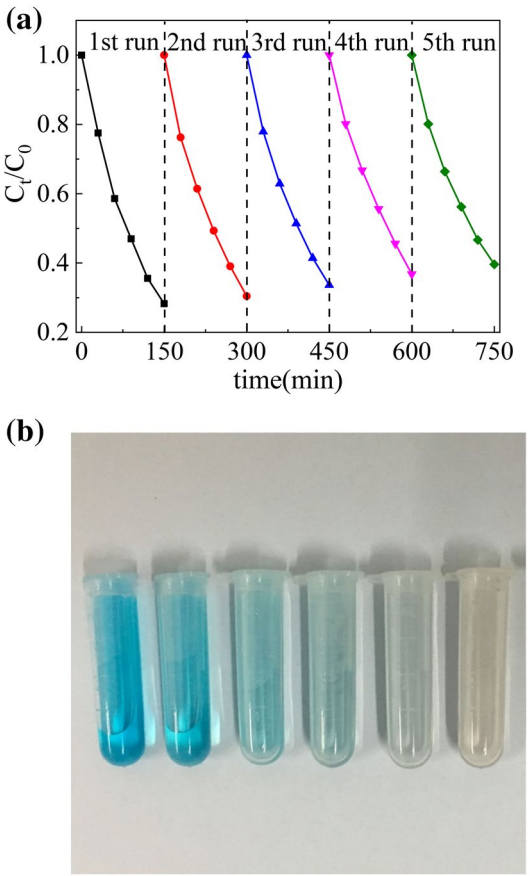

Fig. 10 Recyclability of $MnFe_2O_4$/rGO for photo-Fenton degradation of MB (**a**) and the supernatant obtained at given time intervals (**b**)

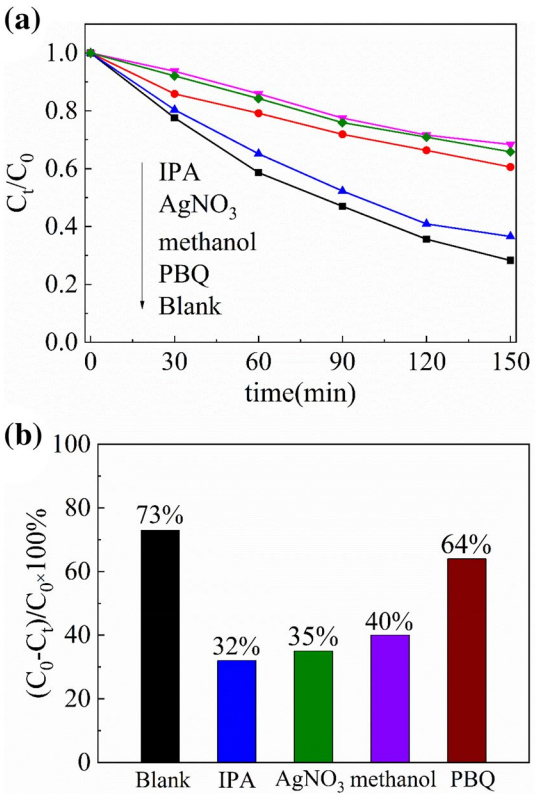

Fig. 11 Photo-Fenton degradation of MB (**a**) and the degradation efficiency (**b**) of $MnFe_2O_4$/rGO with different capture agents

peak is centered at 450–500 nm in $MnFe_2O_4$/rGO, which is basically consistent with pure $MnFe_2O_4$. The luminescence intensity of $MnFe_2O_4$/rGO is weaker than that of $MnFe_2O_4$, which corresponds to a low recombination probability of photogenic charge [13]. Graphene can effectively inhibit the recombination of electron–hole pairs, which improves the photo-Fenton performance of the $MnFe_2O_4$/rGO nanocomposite.

Figure 13 shows the possible photo-Fenton mechanism of $MnFe_2O_4$/rGO nanocomposite degradation of MB based on the above experimental results. The energy band edge position of E_{VB} and E_{CB} for $MnFe_2O_4$/rGO can be determined by the following two equations:

$$E_{VB} = X - E^e + 0.5E_g \quad (1)$$

$$E_{CB} = E_{VB} - E_g, \quad (2)$$

where E_{VB} and E_{CB} are the valence band and conduction band energy, E^e= 4.5 eV represents the free electron energy, X represents the electronegativity of semiconductor materials and E_g is the band gap of sample. The values of CB and

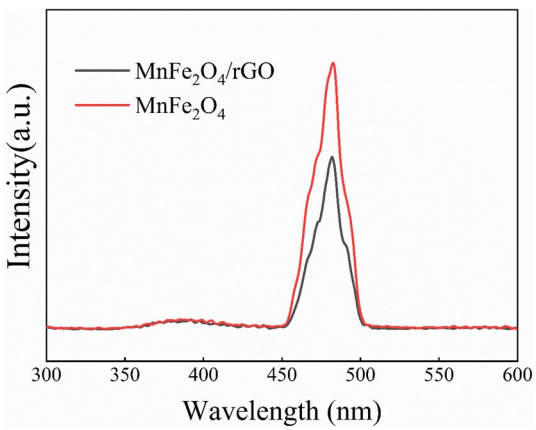

Fig. 12 PL spectra of $MnFe_2O_4$ and $MnFe_2O_4$/rGO

VB for $MnFe_2O_4$/rGO by calculation are −0.01 and +2.43 eV, respectively.

The possible photo-Fenton mechanism of $MnFe_2O_4$/rGO nanocomposite degradation of MB under visible irradiation can be explained in two ways. On the one hand, electron (e^-) are excited to the conduction band (CB), while holes (h^+) are generated in valence band (VB) of $MnFe_2O_4$ under

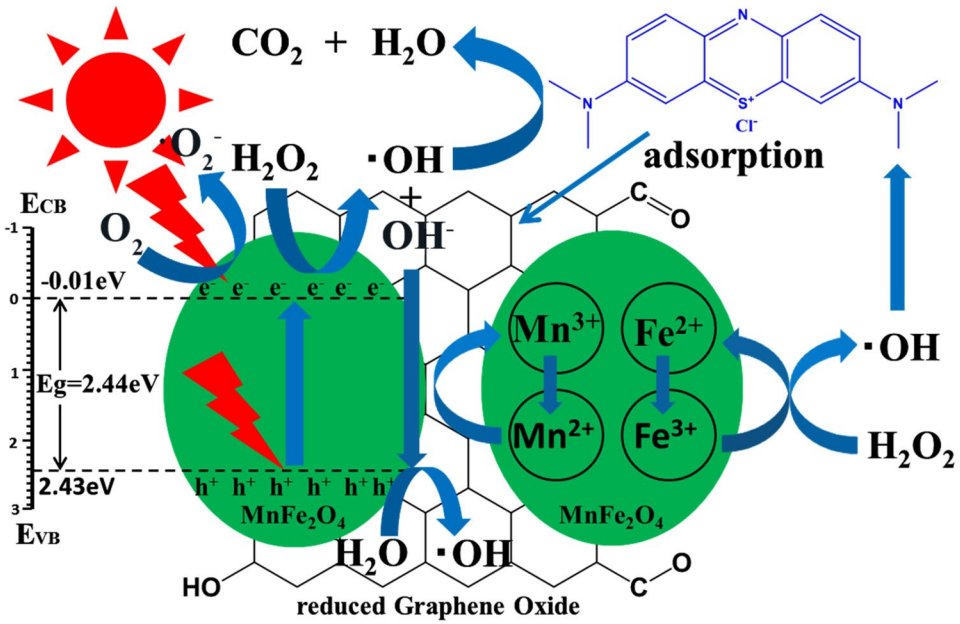

Fig. 13 Schematic illustration of the photo-Fenton mechanism of $MnFe_2O_4$/rGO under simulated sunlight

visible light irradiation. However, only a few photogenerated electron–hole pairs can transfer to the surface of the catalyst to participate in the redox reaction. In contrast, most of electron–hole pairs recombine rapidly for pure $MnFe_2O_4$. Notably, the combinations of electrons and holes are greatly inhibited for $MnFe_2O_4$/rGO composites due to the excellent electron transfer ability of rGO and the chemical bonding of M–O–C on the $MnFe_2O_4$/graphene interface [23]. High-energy electrons (e^-) can react with H_2O to produce hydroxyl radical (·OH), and oxygen (O_2) absorbed on the surface of catalysts can react with electrons to produce superoxide-free radical ($\cdot O^{2-}$). Moreover, the holes (h^+) can react with H_2O_2 to produce ·OH, which further degrades the pollutants into the harmless mineral materials, such as CO_2 and H_2O. On the other hand, the electrical transport of $MnFe_2O_4$/rGO nanocomposites accelerates the effect of Verway hopping ($Mn^{2+} + Fe^{3+} \leftrightarrow Mn^{3+} + Fe^{2+}$), and Fe^{2+} and Mn^{3+} are oxidized or reduced to Fe^{3+} and Mn^{2+} by adding H_2O_2, respectively [18, 19]; especially, a large amount of ·OH is produced in the process of adding H_2O_2, indicating that the electron transfer between the mixed valance Mn^{2+} and Fe^{3+} on octahedral sites for $MnFe_2O_4$/rGO nanocomposites is essential to prevent the recombination of photogenerated electron–hole pairs and enhance the photo-Fenton performance.

4 Conclusions

$MnFe_2O_4$/rGO nanocomposites were synthesized via a facile one-pot hydrothermal method. $MnFe_2O_4$ nanoparticles are cubic spinel structure with uniform particle size and good dispersion, which are loaded on the surface of rGO, partially coated with graphene. The band gap of $MnFe_2O_4$/rGO is narrower than that of pure $MnFe_2O_4$, with redshift phenomenon. The weak luminescence of $MnFe_2O_4$/rGO nanocomposites indicates that the efficient separation of photoexcited electron/hole pairs can improve the photo-Fenton performance. $MnFe_2O_4$/rGO nanocomposites display superior photo-Fenton degradation efficiency of MB under the simulated sunlight, show obvious room temperature ferromagnetism and can be readily recovered by external magnetic field. Meanwhile, $MnFe_2O_4$/rGO nanocomposites possess the best degradation efficiency under the condition of pH 9, 0.5 mL H_2O_2 and with 0.06 g mass fraction for the degradation of MB dye under simulated solar irradiation. The radical scavenger tests demonstrate that ·OH, e^- and h^+ are the main active species and play a decisive role in photo-Fenton degradation of MB for $MnFe_2O_4$/rGO nanocomposites.

Acknowledgements This work was supported by the National Natural Science Foundation of China (51261015), open fund of State Key Laboratory of Silicate Materials for Architectures Wuhan University of Technology (No. SYSJJ2018-20) and Hong Liu First-Class Disciplines Development Program of Lanzhou University of Technology.

References

1. K.E. Sickafus, J.M. Wills, N.W. Grimes, J. Am. Ceram. Soc. **82**, 3279 (2010)
2. G. Gao, W. Feng, W. Su, S. Wang, L. Chen, M. Li, C. Song, Int. J. Electrochem. Sci. **15**, 1426 (2020)
3. M. Li, W. Feng, X. Wang, Int. J. Electrochem. Sci. **15**, 526 (2020)
4. D.B. Miklos, C. Remy, M. Jekel, K.G. Linden, J.E. Drewes, Water. Res. **139**, 118 (2018)

5. W.H. Zhao, Z.Q. Wei, X.J. Wu, X. Wang, Mater. Sci. Semicond. Proc. **88**, 173 (2018)
6. A. Sudhaik, P. Raizada, P. Shandilya, D.Y. Jeong, J.H. Lim, P. Singh, J. Ind. Eng. Chem. **67**, 28 (2018)
7. W.H. Zhao, Z.Q. Wei, L. Zhang, X.J. Wu, X. Wang, Materials. **582**, 1 (2019)
8. M. Mahendiran, J.J. Mathen, K.M. Racik, J. Madhavan, M.V.A. Raj, J. Mater. Sci. **30**, 16099 (2019)
9. T. Hisatomi, J. Kubota, K. Domen, Chem. Soc. Rev. **43**, 7520 (2014)
10. Y. Ma, X.L. Wang, Y.S. Jia, X.B. Chen, H.X. Han, C. Li, Chem. Rev. **114**, 9987 (2014)
11. R.C. Sripriya, M. Mahendiran, J. Madahavan, M.V.A. Raj, Mater. Today **8**, 310 (2019)
12. X. Li, J.G. Yu, J. Low, Y.P. Fang, J. Xiao, X.B. Chen, J. Mater. Chem. A. **3**, 2485 (2015)
13. Y.X. Yan, H. Yang, Z. Yi, T. Xian, X.X. Wang, Environ. Sci. Pollut. Res. **26**, 29020 (2019)
14. N. Sreelekha, K. Subramanyam, D. Amaranatha Reddy, G. Murali, K. Rahul Varma, R.P. Vijayalakshmi, Solid State Sci. **62**, 71 (2016)
15. W.H. Zhao, Z.Q. Wei, X.D. Zhang, M.J. Ding, S.P. Huang, Mater. Res. Bull. **124**, 110749 (2020)
16. Z.M. Wang, H. Ma, C. Zhang, J. Feng, S.Y. Pu, Y.M. Ren, Y. Wang, Chem. Eng. J. **34**, 711 (2017)
17. S.P. Huang, Z.Q. Wei, X.J. Wu, J.W. Shi, Mater. Res. Express **7**, 015025 (2020)
18. F.K. Lotgering, J. Phys.Chem. Solids. **25**, 95 (1964)
19. H. Xu, X. Quan, L. Chen, Chemosphere. **217**, 800 (2019)
20. S. Gautam, P. Shandilya, B. Priya, V. Singh, P. Raizada, R. Rai, M.A. Valente, P. Singh, Sep. Purif. Technol. **172**, 498 (2017)
21. Z.M. Sun, G.Y. Yao, M.Y. Liu, S.L. Zheng, J. Taiwan. Inst. Chem. E. **71**, 501 (2017)
22. V.T. Tran, D.T. Vu, Appl. Phys. A. **124**, 675 (2018)
23. X. Peng, J. Qu, S. Tian, Y. Ding, X. Hai, B. Jiang, M. Wu, J. Qiu, Rsc. Adv. **6**, 104549 (2016)
24. A. Chaudhary, A. Mohammad, S.M. Mobin, Mater. Sci. Eng. B **227**, 136 (2018)
25. M.Q. Qiu, Z.X. Chen, Z.H. Yang, W.M. Li, Y. Tian, W.X. Zhang, Y.S. Xu, H.S. Cheng, Catal. Sci. Technol. **8**, 2557 (2018)
26. J. Feng, Z.Q. Zhang, M.M. Gao, M.Z. Gu, J.X. Wang, W.J. Zeng, Y.Z. Lv, Y.M. Ren, Z.J. Fan, Mater. Chem. Phys. **223**, 758 (2019)
27. N. Khadgi, Y. Li, A.R. Upreti, C. Zhang, W.L. Zhang, Y.M. Wang, D.W. Wang, Photochem. Photobiol. **92**, 238 (2016)
28. S.N. Xiao, D.L. Pan, R. Liang, W.R. Dai, Q.T. Zhang, G.Q. Zhang, C.L. Su, H.X. Li, W. Chen, Appl. Catal. B **236**, 304 (2018)
29. M. Bagherzadeh, R. Kaveh, Photochem. Photobiol. **94**, 1210 (2018)
30. J.L. Jiang, X.X. He, J.F. Du, X.J. Pang, H. Yang, Z.Q. Wei, Mater. Lett. **220**, 178 (2018)
31. T.T. Bi, H.Q. Fang, J.L. Jiang, X.X. He, X. Zhen, H. Yang, Z.Q. Wei, Z.F. Jia, J. Alloy. Compd. **787**, 759 (2019)
32. Y. Huang, Y.L. Liang, Y.F. Rao, D.D. Zhu, J.J. Cao, Z.X. Shen, W.K. Ho, S.C. Lee, Sci. Technol. **51**, 2924 (2017)
33. Y.D. Lu, Y.P. Feng, F.L. Wang, X.G. Zou, Z.F. Chen, P. Chen, H.J. Liu, Y.H. Su, Q.X. Zhang, G.G. Liu, J. Photochem. Photobiol. A **353**, 10 (2018)
34. Y.L. Guo, L.L. Zhang, X.Y. Liu, B. Li, D. Tang, W.S. Liu, W.W. Qin, J. Mater. Chem. A. **4**, 4044 (2016)
35. X. Huang, L. Liu, Z. Xi, H. Zheng, W. Dong, G. Wang, Mater. Chem. Phys. **231**, 68 (2019)
36. A. Mishra, V. Sharma, T. Mohanty, B.K. Kuanr, J. Alloy. Compd. **790**, 983 (2019)
37. Y. Yao, Y. Cai, F. Lu, F. Wei, X. Wang, S. Wang, J. Hazard. Mater. **270**, 61 (2014)
38. N.U. Yamaguchi, R. Bergamasco, S. Hamoudi, Chem. Eng. J. **295**, 391 (2016)
39. P.H. Luo, X.F. Guan, Y.L. Yu, X.Y. Li, Chem. Phys. Lett. **690**, 129 (2017)
40. M.S. Cuevas, I. Oller, A. Agüera, J. Sánche-Pérez, S. Malato, Chem. Eng. J. **318**, 161 (2017)
41. P.J. Wang, L.Q. Wang, Q. Sun, S.B. Qiu, Y. Liu, X.B. Zhang, X.L. Liu, L.H. Zheng, Mater. Lett. **183**, 61 (2016)
42. X.L. Zhu, Z.Q. Wei, W.H. Zhao, X.D. Zhang, L. Zhang, X. Wang, J. Electron. Mater. **47**, 6428 (2018)
43. W.H. Zhao, Z.Q. Wei, X.L. Zhu, X.D. Zhang, J.L. Jiang, Int. J. Mater. Res. **109**, 405 (2018)
44. X.L. Zhu, Z.Q. Wei, L. Ma, J.H. Liang, X.D. Zhang, Mater. Sci. **43**, 1 (2020)
45. Y.X. Yan, H. Yang, Z. Yi, T. Xian, R.S. Li, X.X. Wang, Desalin. Water Treat. **170**, 349 (2019)